Piezoresistive Properties of Suspended Graphene Membranes under Uniaxial and Biaxial Strain in Nanoelectromechanical Pressure Sensors

A.D. Smith[1], F. Niklaus[1], A. Paussa[2], S. Schröder[1], A.C. Fischer[1], M. Sterner[1], S. Wagner[3], S. Vaziri[1], F. Forsberg[1], D. Esseni[2], M. Östling[1], and M.C. Lemme[1,3]

[1]KTH Royal Institute of Technology, Stockholm, Sweden
[2]DIEGM, University of Udine, Italy
[3]University of Siegen, Germany

Supporting Information

Experimental Setup

Figure S1 shows a schematic of the measurement setup for measuring the resistance of the devices. The Wheatstone bridge is made up of two fixed resistances, a potentiometer, and the graphene pressure sensor device. A square wave output signal is then filtered through a low pass filter and into an amplifier. It is then passed through another low pass filter to an analog to digital converter. From there, the digital signal is sent to LabView. The recorded signal output from Labview represents only those portions of the signal which are measured during the square wave pulses in a method similar to previous reports.[1]

Raman Spectroscopy

Raman spectra were performed for a number of samples with transferred graphene at different locations on the graphene layer (Figure S2). The Raman spectra confirm the presence of graphene over the sample as well as in the cavity region. The Raman spectrum of graphene shows G and 2D peaks at approximately 1600 cm^{-1} and 2700 cm^{-1}, respectively.[2] In S2a, 6 Raman spectra are displayed while Figure S2b displays an SEM image of a graphene patch over a cavity. The circles represent the approximate location of the Raman spot where the measurement was performed. In the case of the Raman spectra over the cavity, there appears to be a slight shift of the peaks which could be indicative of a slight strain.[3]

Capacitive Coupling

From COMSOL simulations, capacitance normalized per unit area was calculated for the graphene as it is strained. This was done by taking the average deflection at a given pressure and converting it into a capacitance using Eq. 1. This was then compared to the average strain at the given deflection. These calculations are shown in Fig. S2a. There are several important things to notice about the simulation. First, the change in capacitance for our devices is nearly 5 times less than the change in capacitance for Huang.[4] This is significant since the dielectric thickness is 5 times greater for our devices than for Huang and our dielectric layer is comprised entirely of air while in Huang it is a combination of air and SiO_2 (which has a substantially higher permittivity constant of 3.9).

$$C_{ox} = \frac{\varepsilon_r \varepsilon_0}{t} \quad (1)$$

The other important thing to notice is that in the Huang experiment, the membrane is being pressed into the cavity (top inset of Fig. S2a) causing the capacitance to increase due to a decrease in distance between electrodes. In contrast, our experiment has air inside the cavity pressing the graphene outward (bottom inset of Fig. S2a), thereby further decreasing the capacitance. This is why the relative normalized change in capacitance is negative for increasing strains in our case but positive for increasing strains (Fig. S2a) in Huang *et al.*[4]

Eq. 3 shows the carrier concentration for graphene knowing the SiO_2 capacitance, C_{ox}, which we extract from the COMSOL simulation, the gate voltage, V_{gs} , and the point of minimum conductivity, V_D. $V_{gs} - V_D$ represents an effective potential in the substrate caused by trapped charges. The

capacitance C_{ox} will then change as the strain changes due to different deflections which in turn result in different effective values of the distance *t* between the electrodes in Eq.2. The variations of C_{ox} will correspondingly change the charge carrier density according to Eq.3 and thereby the resistance.

$$qN = C_{ox}(V_{gs} - V_D) \qquad (2)$$

Then, the lowest intrinsic charge carrier density derived from Morozov *et al.*[5] was used to arrive at charge densities as a function of capacitance for different gate voltages. The lowest value was chosen in order to provide the greatest % change in resistance due to the coupling and therefore the most conservative estimate. Let us now reconsider Eq.3 of the paper to express R_2 and set the strain to zero because we want to isolate the possible effect on the resistance of the capacitance change

$$R_2 = \rho \frac{L'}{W_t'} = \frac{1}{2q(N_i+N)\mu_e}\frac{L}{W_t} \qquad (3)$$

where the electron density N_e has been expressed as the sum of the the intrinsic density N_i, (i.e. the carrier density corresponding to no trapped charges), plus the density N induced by trapped charges estimated by Eq.3 in terms of an effective gate biasing effect. Such a charge density contribution changes with the capacitance C_{ox} and we denote by N_0 and N_1 the charge density corresponding respectively to the nominal C_{ox} value (i.e. no strain induced membrane deflection) and the C_{ox} value modified by the membrane deflection produced by the pressure in the cavity. If we now consider the R_2 percent change induced by the C_{ox} variation alone, all terms are constant in Eq.3 except for the carrier density term and therefore We we can readily express the R_2 percent change as

$$\frac{R_2-R_0}{R_0} \times 100 = \left[\frac{(N_i+N_0)}{(N_i+N_1)} - 1\right] \times 100 \qquad (4)$$

The results for the R_2 percent changes obtained from Eq.4 are shown in Fig. S2b for different (V_{gs}-V_D) values ranging from 100 mV to 10 V, thereby emulating different values of trapped/fixed charges. Note that even at 10 V gate biasing, the effect of capacitive coupling is dwarfed by the effect, which we see in our data based on the most conservative estimates performed. Furthermore, our devices are not biased. Therefore, while there is likely some influence of capacitive coupling due to trapped/fixed charges in the substrate, this influence should be very minimal.

Strain Direction

We can extract both e_{xx} and e_{yy} strain components for each element in the FEA analysis over the membrane (Figure S3). The magnitude of these components is then compared for both the uniaxial and biaxial cases shown in Figure S3. The rectangular membrane results in near uniaxial strain, which approaches true uniaxial strain the larger the width/length aspect ratio of the cavity. The circular membrane results in biaxial strain.

Gauge Factor Strain Independence

Gauge factor extractions were not only related to pressure changes, but also strain changes. Figure S4 compares the gauge factors for each of the measured devices to changes in membrane strain. Note that, as the strain across the membrane changes, there is little change in the gauge factor. This

result is predicted by LBTE simulation for both uniaxial and biaxial strains (blue and red dots, respectively).

Comparison to Control Device

Several control devices have been measured which are identical to the pressure sensor devices with the exception of the cavity region. Figure S5 shows the signal response of the suspended membrane devices compared to such a control device. Note that, in the case of the non-cavity device, there is virtually no signal response. This demonstrates that the presence of the suspended membrane is the primary factor in the device pressure sensitivity.

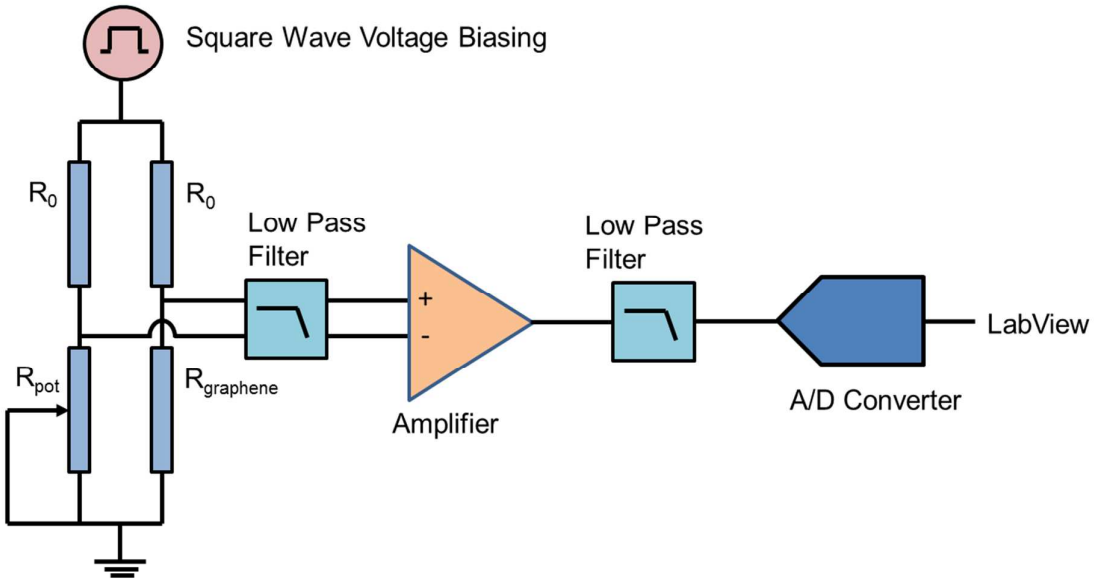

Figure S1: Measurement setup for measuring the resistance of the graphene membrane-based pressure sensors at different pressures inside the pressure chamber. The graphene resistor $R_{Graphene}$ is placed in a Wheatstone bridge configuration.

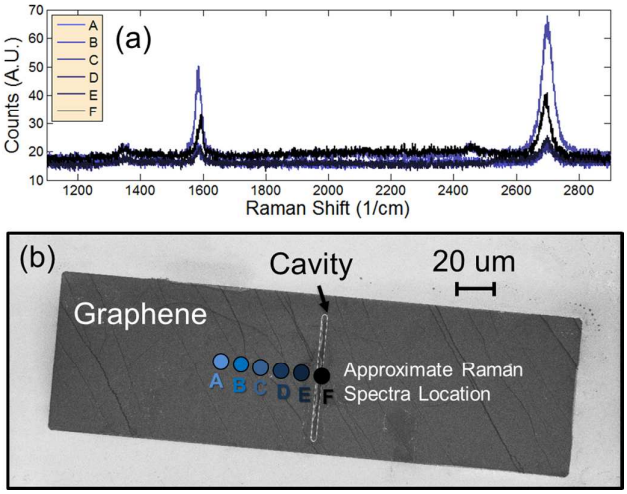

Figure S2: a) Raman spectra at different locations over a graphene patch. b) SEM image illustrating approximate locations where Raman spectra were measured (results adapted from Smith *et al.*).[3]

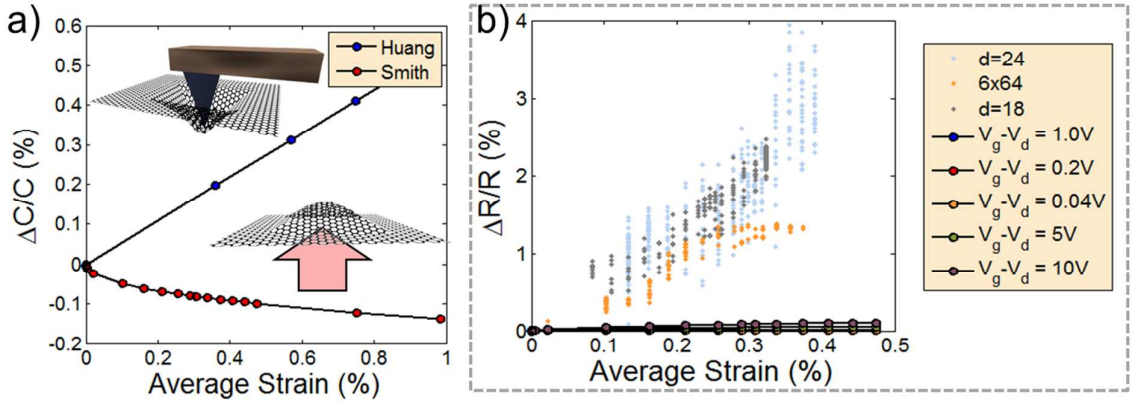

Figure S3: a) shows the change in capacitance versus strain for our data compared with Huang *et al.* The top inset shows the experimental setup in Huang *et al.* and the bottom inset shows the experimental setup of our devices. b) Our experimental data for % change in resistance compared with simulated changes in resistance due to only capacitive coupling for several different gate voltages.

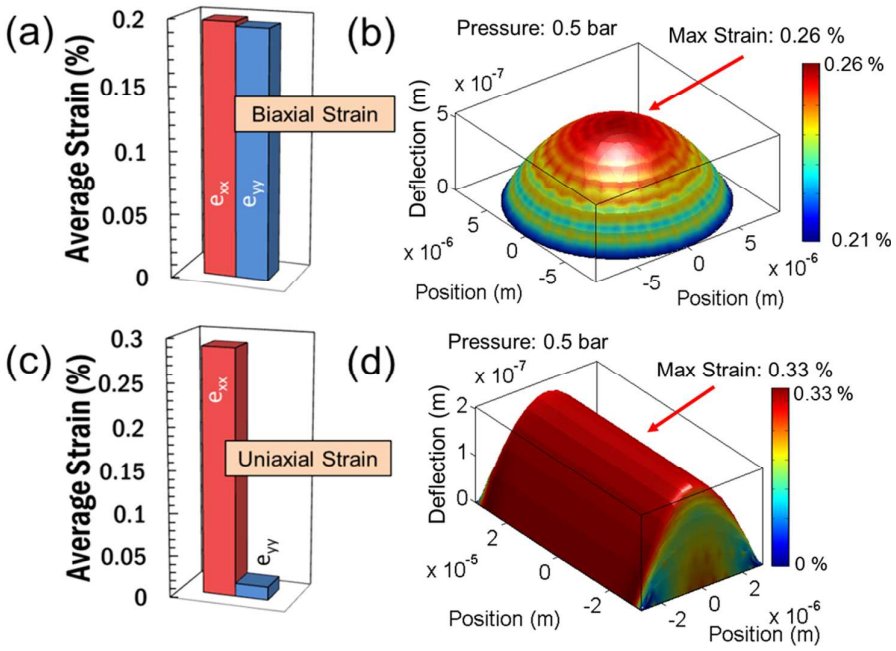

Figure S4: a) average strain of a biaxially strained 18 µm circular membrane. b) FEA strain model of the 18 µm biaxial membrane. Red indicates regions of larger strain. c) Average strain of a uniaxially strained 6x64 µm rectangular membrane. d) FEA strain model of the same membrane. Red indicates regions of larger strain.

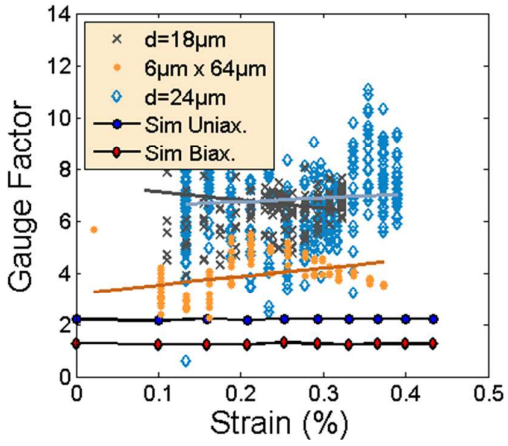

Figure S5: Gauge factor comparison for different strains.

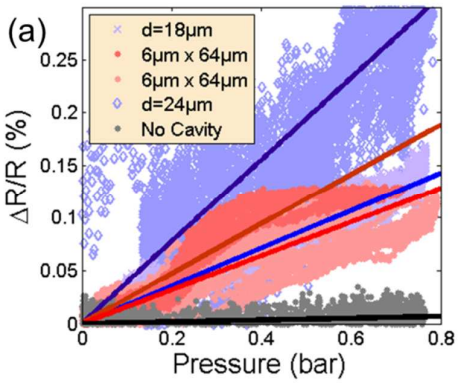

Figure S6: Comparison of signal responses for 4 devices compared to a reference device (no cavity).

References

(1) Smith, A. D.; Niklaus, F.; Paussa, A.; Vaziri, S.; Fischer, A. C.; Sterner, M.; Forsberg, F.; Delin, A.; Esseni, D.; Palestri, P.; Östling, M.; Lemme, M. C. Electromechanical Piezoresistive Sensing in Suspended Graphene Membranes. *Nano Lett.* **2013**, *13*, 3237–3242.

(2) Malard, L. M.; Pimenta, M. A.; Dresselhaus, G.; Dresselhaus, M. S. Raman Spectroscopy in Graphene. *Phys. Rep.* **2009**, *473*, 51–87.

(3) Smith, A. D.; Vaziri, S.; Delin, A.; Ostling, M.; Lemme, M. C. Strain Engineering in Suspended Graphene Devices for Pressure Sensor Applications. In *Ultimate Integration on Silicon (ULIS), 2012 13th International Conference on*; IEEE, 2012; pp. 21–24.

(4) Huang, M.; Pascal, T. A.; Kim, H.; Goddard III, W. A.; Greer, J. R. Electronic- Mechanical Coupling in Graphene from in Situ Nanoindentation Experiments and Multiscale Atomistic Simulations. *Nano Lett.* **2011**, *11*, 1241–1246.

(5) Morozov, S. V.; Novoselov, K. S.; Katsnelson, M. I.; Schedin, F.; Elias, D. C.; Jaszczak, J. A.; Geim, A. K. Giant Intrinsic Carrier Mobilities in Graphene and Its Bilayer. *Phys. Rev. Lett.* **2008**, *100*, 16602.